Supporting Information

Transparent Conductive Two-Dimensional Titanium Carbide Epitaxial Thin Films

*Joseph Halim,[†,‡,§] Maria R. Lukatskaya,[†,‡]Kevin M. Cook,[†,‡] Jun Lu,[§] Cole R. Smith,[†]Lars-ÅkeNäslund,[§] Steven J. May,[†] Lars Hultman,[§]Yury Gogotsi,[†,‡ *,] Per Eklund,[§,*] and Michel W. Barsoum[†,§,*]*

[†]Department of Materials Science & Engineering, Drexel University, Philadelphia, PA 19104, USA.

[‡]A.J. Drexel Nanomaterials Institute, Drexel University, Philadelphia, PA 19104, USA. Department of Materials Science & Engineering, Drexel University, Philadelphia, PA 19104, USA.

[§]Thin Film Physics Division, Department of Physics, Chemistry and Biology (IFM), Linköping University, SE-581 83, Linköping, Sweden.

barsoumw@drexel.edu; perek@ifm.liu.se; gogotsi@drexel.edu

I. X-ray reflectometry and thickness determination

Films' thickness has been determined from XRR for Ti_3AlC_2 films, before and after etching, deposited for 5 and 10 min, examples of the XRR data and their fittings shown in Figures S1, and S2. For Ti_3AlC_2 film deposited for 30 mins, thicknesses before and after etching were obtained by direct measurement in TEM (Figures 2a-c, and Figure S9c). Figure S1 shows the measured X-Ray reflectometry for Ti_3AlC_2 (black curve), and best-fitted simulation from TiC incubation layer/Ti_3AlC_2 (red curve): for a film deposited for 5 min (Figure S1a) giving a thickness of 15.2 ± 0.5 nm and a film deposited for 10 min (Figure S1b) giving a thickness of 27.7 ± 0.8 nm. Figure S1c shows the relationship between the thickness of Ti_3AlC_2, $Ti_3C_2T_x$ and $Ti_3C_2T_x$-IC and deposition time of Ti_3AlC_2. Films deposited for 20 min: their thickness before and after etching was obtained from interpolation (Figure S3c).
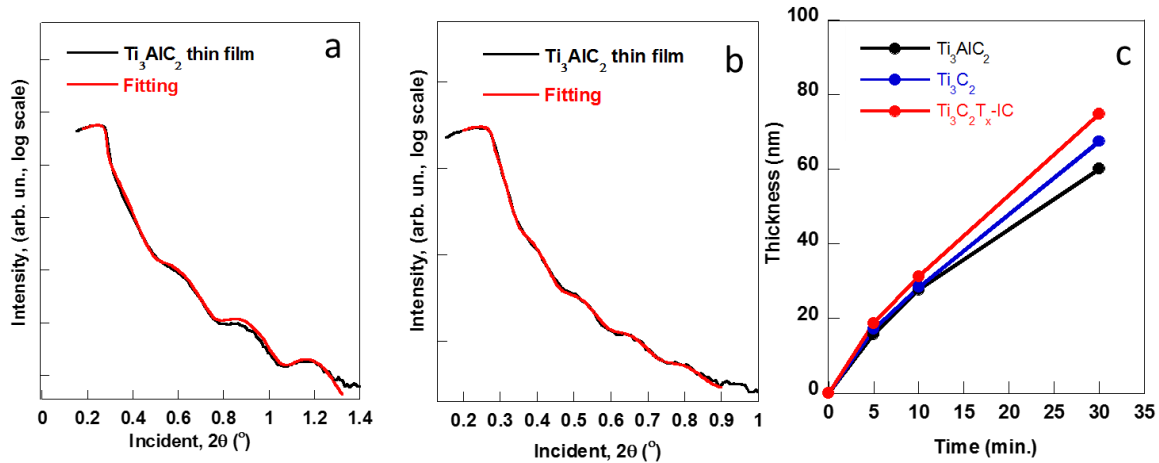

Figure S1. Measured X-Ray reflectometry for (a) Ti_3AlC_2 sputtered for 5 min and, (b) Ti_3AlC_2 sputtered for 10 min, Ti_3AlC_2 (black curve), and best fit simulation for TiC incubation layer/ Ti_3AlC_2 (red curve) and (c) Thickness *vs.* deposition time of Ti_3AlC_2 for Ti_3AlC_2, $Ti_3C_2T_x$ and $Ti_3C_2T_x$-IC.

II. XPS analysis of Ti_3AlC_2, $Ti_3C_2T_x$, and $Ti_3C_2T_x$-IC

Analysis of the high-resolution XPS spectra was performed through peak fitting using symmetric Gaussian-Lorentzian curves resting on a Shirley background.

Fig. S2 presents the Ti 2p, C 1s, and Al 2p regions for the Ti_3AlC_2 thin film together with the obtained Shirley background and Gaussian-Lorentzian curves for each region. In the Ti 2p region (Figure S2a), which contains both the $2p_{1/2}$ and the $2p_{3/2}$ spin-orbit split components, the XPS spectrum could be best fit with four pairs of Gaussian-Lorentzian curves, where each pair is the $2p_{1/2}$ and the $2p_{3/2}$ component that we assign to Ti-Al, Ti-C, Ti(II) oxide, and Ti(III) oxide, respectively.[1-4]

The C 1s region (Figure S2b) could be fit with four Gaussian-Lorentzian curves. The low binding energy feature is a sharp asymmetric peak that is assigned to the Ti-C bond.[1,2] The asymmetry is due to extrinsic energy losses caused by delocalized states. This asymmetry, in turn, required the Ti-C XPS peak to be fit with two symmetric Gaussian-Lorentzian curves. In addition to the Ti-C peak there are two peaks assigned to surface hydrocarbon (-CH_2- & -CH_3) and carboxylate (-COO)[5] contamination common for samples exposed to laboratory air.[6]

In the Al 2p region (Figure S2c) the low binding energy feature contains the $2p_{1/2}$ and the $2p_{3/2}$ spin-orbit split components assigned to Ti-Al.[3] The high binding energy feature is assigned to an aluminum oxide components,[2] fitted with a symmetric Gaussian-Lorentzian curve, due to surface oxidation which is common for MAX phase materials.[2] The results obtained from the peak fitting of the Ti_3AlC_2 thin film are summarized in Table S1.
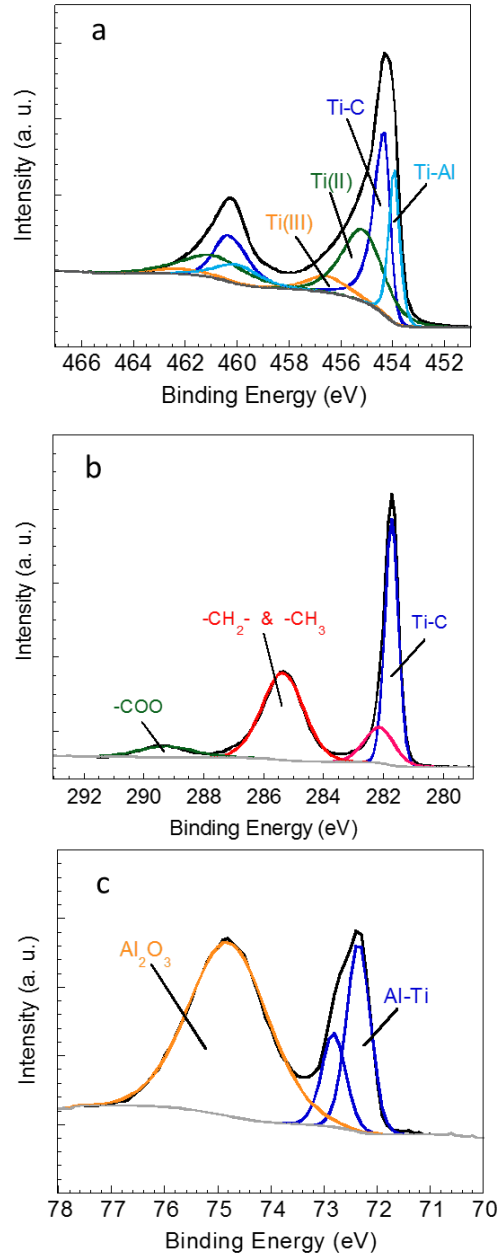

Figure S2. Deconvolution of high resolution XPS spectra for elements in Ti_3AlC_2 films. (a) Ti 2p, (b) C 1s and (c) Al 2p XPS high resolution spectra for Ti_3AlC_2 thin films.

Table S1. Ti$_3$AlC$_2$ XPS peak fitting results. Parameters obtained from the peak fitting of the Ti$_3$AlC$_2$ thin film XPS spectra using symmetric Gaussian-Lorentzian curves.

	BE [eV][a]	fwhm [eV][a]	Fraction	Assigned to	Reference
Ti 2p$_{3/2}$	453.9 (459.9)	0.5 (2.0)	0.20	Ti-Al	3
(2p$_{1/2}$)	454.3 (460.3)	0.5 (1.3)	0.37	Ti-C	1, 2
					4
	455.2 (460.9)	1.9 (3.0)	0.35	Ti(II) oxide	4
	456.5 (462.1)	1.9 (3.0)	0.08	Ti(III) oxide	
C 1s	281.7	0.5	0.38	Ti-C	1, 2
	282.1	1.2	0.13	Ti-C	
	285.3	1.7	0.43	-CH$_2$- & -CH$_3$	5
	289.3	1.7	0.06	-COO	5
Al 2p$_{3/2}$	72.4 (72.8)	0.5 (0.5)	0.33	Ti-Al	3
(2p$_{1/2}$)	74.8 (74.8)	1.7	0.66	Al$_2$O$_3$	5

[a]Values in parenthesis corresponds to the 2p$_{1/2}$ component.

Figures S3a-d and Figures S3e-h represent the Ti 2p, C 1s, O 1s, and F 1s regions for the Ti$_3$C$_2$T$_x$ thin film and the Ti$_3$C$_2$T$_x$-IC thin film, respectively. For both MXene thin films, the XPS spectrum of the Ti 2p region (Figures S3a, and S3e) could be best fitted with five pairs of Gaussian-Lorentzian curves, where each pair is the 2p$_{1/2}$ and the 2p$_{3/2}$ component that we assign to Ti-C, Ti(II) oxide, Ti(III) oxide, Ti(IV) oxide, and Ti-F, respectively.[3-5,7-9] The C 1s region for both MXene thin films (Figures S3b, and S3f) shows features assigned to Ti-C,[1, 2] hydrocarbons (-CH$_2$- & CH$_3$-), and carboxylates (-COO). In this case intense contributions from graphite (C-C) and alcohol (C-O) formation are also present.[5]

The O 1s region for both MXene thin films (Figures S3c, and S3g) could be fit by two components assigned to titanium oxide: one component for stoichiometric TiO$_2$ and one component for sub-stoichiometric TiO$_x$.[9] The O 1s region also suggests Ti-OH formation and H$_2$O uptake.[9]
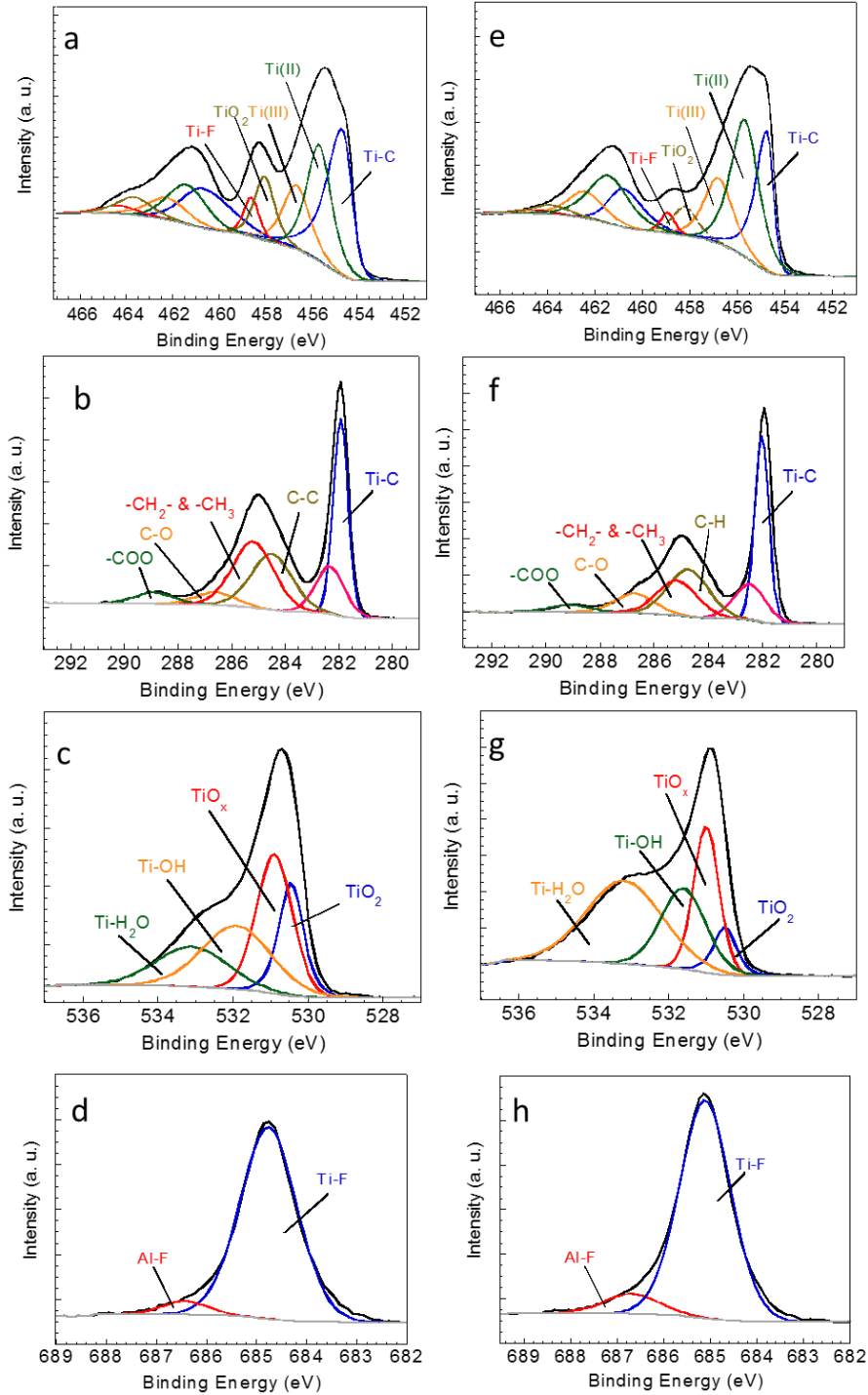
4

Figure S3. Deconvolution of high resolution XPS spectra for elements in $Ti_3C_2T_x$, and $Ti_3C_2T_x$-IC. (a) Ti 2p, (b) C 1s, (c) O 1s and, (d) F 1s regions for $Ti_3C_2T_x$ C; and, (e) Ti 2p; f, (f) 1s, (g) O 1s and, (h) F1s regions for $Ti_3C_2T_x$-IC thin films.

The F 1s region for both MXene thin films (Figs. S3d and S3h) shows a dominating contribution from fluorinated titanium,[8] Ti-F, but also a small component assigned to aluminum fluoride,[10] Al-F, which is corroborated by the appearance of a weak feature at

73.6 eV in the Al 2p spectra shown in Figure 2b. The results obtained from the peak fitting of the $Ti_3C_2T_x$ thin film and the $Ti_3C_2T_x$-IC thin film are summarized in Tables S2 and S3.

Table S2. $Ti_3C_2T_x$ XPS peak fitting result. Parameters obtained from the peak fitting of the $Ti_3C_2T_x$ thin film XPS spectra using symmetric Gaussian-Lorentzian curves.

	BE [eV][a]	fwhm [eV][a]	Fraction	Assigned to	Reference
Ti $2p_{3/2}$ ($2p_{1/2}$)	454.6 (460.7)	0.9 (2.2)	0.37	Ti-C	[1, 2, 7]
	455.6 (460.9)	1.3 (2.0)	0.28	Ti(II) oxide	[4, 7]
	456.6 (462.2)	1.4 (2.0)	0.17	Ti(III) oxide	[7]
	458.0 (463.7)	1.0 (1.8)	0.12	Ti(IV) oxide	[10,9]
	458.6 (464.3)	0.8 (1.8)	0.06	Ti-F	[8]
C 1s	281.9	0.6	0.25	Ti-C	[1, 2]
	282.3	1.3	0.15	Ti-C	
	284.5	1.6	0.15	C-C	[5]
	285.2	1.6	0.34	-CH_2- & -CH_3	[5]
	286 .6	1.6	0.07	C-O	[5]
	288.9	1.6	0.04	-COO	[5]
O 1s	530.5	0.8	0.21	TiO_2	[9]
	531.0	1.1	0.33	TiO_x	[9]
	531.8	2.0	0.25	Ti-OH	[9]
	533	2.2	0.21	Ti-H_2O	[9]
F 1s	684.7	1.3	0.95	Ti-F	[8]
	686.4	1.1	0.05	Al-F	[10]

[a]Values in parenthesis corresponds to the $2p_{1/2}$ component.

Table S3. $Ti_3C_2T_x$-IC XPS peak fitting result. Parameters obtained from the peak fitting of the $Ti_3C_2T_x$-IC thin film XPS spectra using symmetric Gaussian-Lorentzian curves.

	BE [eV][a]	fwhm [eV][a]	Fraction	Assigned to	Reference
Ti $2p_{3/2}$	454.7 (460.8)	0.7 (1.5)	0.29	Ti-C	[1, 2, 7]
($2p_{1/2}$)	455.7 (461.4)	1.4 (2.0)	0.41	Ti(II) oxide	[4, 7]
	456.8 (462.4)	1.4 (1.8)	0.20	Ti(III) oxide	[7]
	458.2 (463.9)	1.2 (1.9)	0.07	Ti(IV) oxide	[10,9]
	458.9 (464.6)	0.7 (1.9)	0.03	Ti-F	[8]
C 1s	281.9	0.6	0.29	Ti-C	[1, 2]
	282.3	1.4	0.14	Ti-C	
	284.6	1.8	0.21	C-C	[5]
	285.2	1.8	0.21	C-H	[5]
	286.6	1.8	0.11	C-O	[5]
	289.0	1.8	0.04	-COO	[5]
O 1s	530.5	0.7	0.08	TiO_2	[9]
	530.9	0.8	0.25	TiO_x	[9]
	532.5	1.4	0.25	Ti-OH	[9]
	533.1	2.4	0.42	Ti-H_2O	[9]
F 1s	685.3	1.3	0.91	Ti-F	[8]
	686.7[b]	1.4	0.09	Al-F	[10]

[a]Values in parenthesis corresponds to the $2p_{1/2}$ component.
[b]The peak for the aluminum fluoride component shifts to a higher binding energy compared to that for $Ti_3C_2T_x$, while its FWHM maximum increases, which may be due to the formation of $(NH_4)_3AlF_6$ rather than AlF_3 as indicted by XRD in Figure S6.

The high-resolution XPS spectra of the Ti 2p and C 1s regions for the Ti_3AlC_2, $Ti_3C_2T_x$, and $Ti_3C_2T_x$-IC thin films show that the removal of Al causes a shift of the Ti-C contribution in the Ti 2p and C 1s XPS spectra toward higher binding energies, indicative of a loss of charge, and a concomitant charge redistribution within the material. Note that this decrease of charge is not due to the removal of Al atoms, because the latter needs to leave behind the charge they gained when forming Ti_3AlC_2. The charge redistribution is instead a consequence of the higher electronegativities of the OH, O and F surface functional groups, as mentioned in the main text.

In addition there is a slight shift to higher binding energies for the Ti 2p spectrum of the $Ti_3C_2T_x$-IC thin film compared to the corresponding spectrum of $Ti_3C_2T_x$. Since the matching C 1s spectra do not show any changes in the binding energies, the observed binding energy shift could be due to the intercalated nitrogen species (Figure 2e) interacting with the surface of the $Ti_3C_2T_x$-IC thin film.

The peak fitting of the XPS high-resolution spectra suggests the chemical compositions to be $Ti_3C_{2.2}O_2F_{0.6}$ and $Ti_3C_{2.3}O_{1.2}F_{0.7}N_{0.2}$ for $Ti_3C_2T_x$ and Ti_3C_2-IC, respectively. Fitted peaks that correspond to surface oxidation and contamination, i.e. TiO_2, H_2O, hydrocarbons, alcohols, carboxylates, and aluminum fluoride, are not included in these elemental quantifications. The obtained quantification data indicates that the etching of Ti_3AlC_2, using HF or NH_4HF_2, provides near-stoichiometric Ti_3C_2 2D-stuctures, surface terminated with a mixture of fluoride- and hydroxyl groups. Additionally, etching in NH_4HF_2 results in the intercalation of the nitrogen species, NH_4^+ and NH_3.[11,12]

III. XRD analysis of the byproducts from etching Ti_3AlC_2 with NH_4HF_2

One half of a gram of Ti_3AlC_2 powder (the method of preparation is described elsewhere[13]) were soaked in 5ml of 1M NH_4HF_2 solution at room temperature. The mixture was left untouched until the solvent evaporated. XRD diffraction of the dry powders (Figure S4) indicates the existence of two byproduct compounds $(NH_4)_3AlF_6$ (PDF# 22-1036) and $AlF_3.3H_2O$ (PDF# 46-1459) comparing the intensity of the maximum peaks for both gives a ratio of about 7:1 respectively. It follows that the major byproduct from etching Ti_3AlC_2 with NH_4HF_2 is $(NH_4)_3AlF_6$.

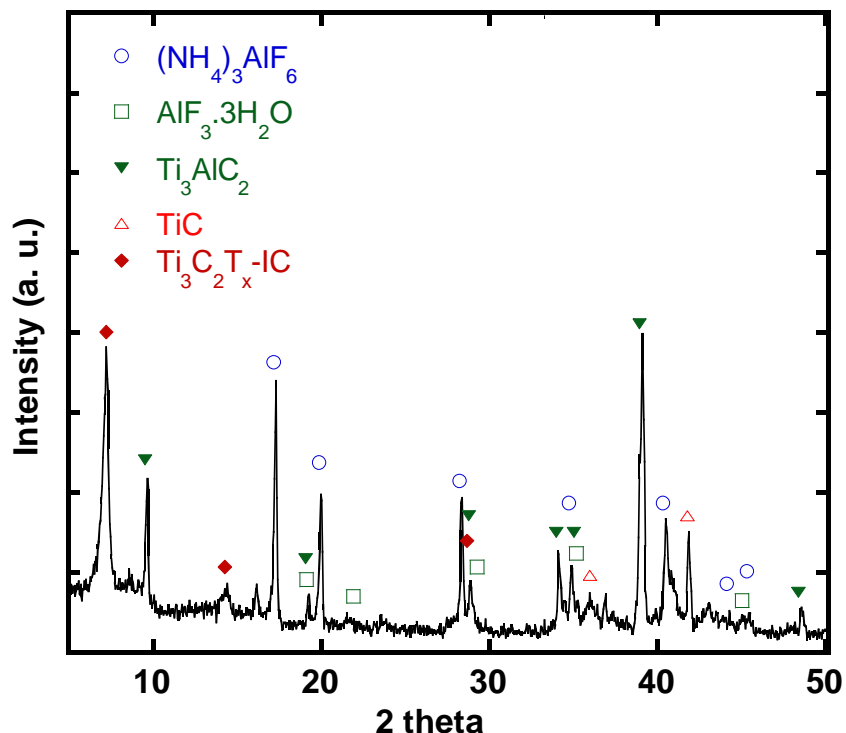**Figure S4:** X-Ray diffraction pattern of $Ti_3C_2T_x$ intercalated MXene ($Ti_3C_2T_x$-IC) after etching Ti_3AlC_2 powder with 1M NH_4HF_2, and allowing the mixture to sit until the solvent dried. In contrast to our previous work, here the resulting salt was not washed away with water. The XRD pattern also includes peaks associated with un-reacted Ti_3AlC_2 and TiC present as an impurity in the as-received powders.

IV. Intercalation and de-intercalation of $Ti_3C_2T_x$

In order to verify the assumption that intercalation is the pertinent mechanism, Ti_3C_2 powder (the method of preparation is described elsewhere[13]) were immersed in 1 M of NH_4F or in 5 M NH_4OH for 24 h at room temperature while stirring. XRD patterns before and after treatment, shown in Fig. S5a, confirm that the increase in c, from 19.8 Å to 25 Å, in both solutions is similar to that observed when NH_4HF_2 was used as etchant. It is thus reasonable to assume that, intercalant compound should be the common species between NH_4HF_2, NH_4F and NH_4OH, viz. NH_4^+.

To investigate the reversibility of the intercalation process, a 43 nm nominal thickness $Ti_3C_2T_x$-IC film was heated in a vacuum at 250 °C for 90 min. The XRD patterns for the film before and after de-intercalation are compared in Figure S5b. After the vacuum treatment, the (0002) peak shifts to an angle that corresponds to a c lattice parameter of 21 Å. It is thus possible to de-intercalate ammonia from $Ti_3C_2T_x$-IC. This value is also quite similar to, the lattice parameter obtained from SAED pattern shown in Figure 3e, suggesting that the TEM sample was partially de-intercalated during the sample preparation.
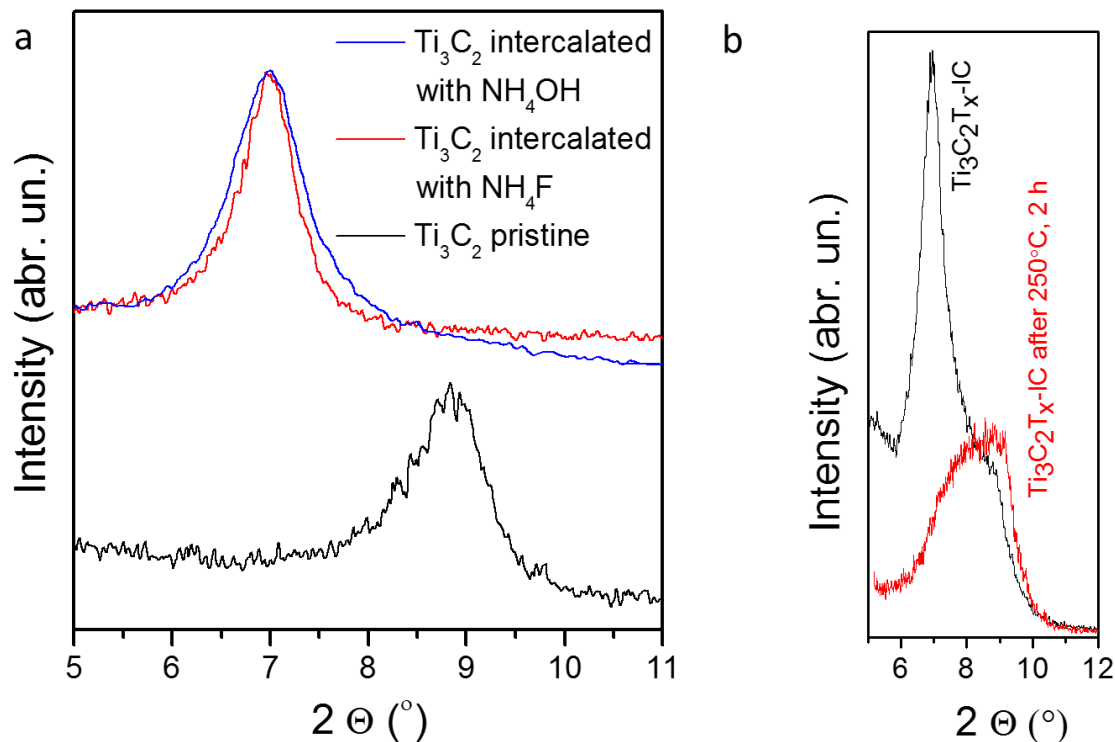
Figure S5. (a) X-Ray diffraction pattern of initial MXene ($Ti_3C_2T_x$) powder (black curve), and after 24 h treatment at room temperature with 1 M NH_4F (red curve) and 5 M NH_4OH (blue curve). (b) $Ti_3C_2T_x$-IC film of 43 nm nominal thickness before and after heating in vacuum at 250 °C for 2 h.

V. Optimization of the etching process

The resistivities of all films increased with increase in etching times. Table S4 lists the resistivities of $Ti_3C_2T_x$ films produced by HF etching for samples, of the same nominal thicknesses, etched for different times. For example, the resistivities of Ti_3AlC_2 films, 60 nm nominal thick, etched for 160 mins and 360 mins were 1.8 μΩm and 3.4 μΩm, respectively.

The etching time required to fully transform the Ti_3AlC_2 films to MXenes was determined by repeatedly measuring the XRD diffraction patterns, of a given film, after successive etching steps until the XRD peaks belonging to Ti_3AlC_2 disappeared (Figure S6). This procedure was adopted in order to compare the properties of all etched films at the point all the Al layers were etched out. Said otherwise, the etching times varied from film to film. The dependence is not linear, however. For example, the etching times for Ti_3AlC_2 films of nominal thicknesses 15 and 28 nm were 10 and 15 mins, respectively. Similarly, at 150 min and 160 min, the time needed to fully etch 15 nm and 28 nm thick Ti_3AlC_2 films in NH_4HF_2, were quite comparable (See Table 1).

A perusal of the results shown in Tables 1 and S4 suggest that the final resistivities one obtains is a complicated function of film thickness, etching times and the nature of the etchant. On the one hand, thin films are more resistive than their thicker counterparts. It is this variability - reflected in Table 1 - that is most probably responsible for some of the

10

anomalies observed. For example, the etching times for $Ti_3C_2T_x$ films of nominal thicknesses of 15, 28 and 43 nm were 10, 15 and 60 min, respectively.

Table S4: Resistivity of Ti_3AlC_2 films after etching in 50% HF for various times. The thicknesses listed in the first column are thicknesses before etching

Thickness [nm]	Etching time [minutes]	Resistivity [$\mu\Omega m$]
10	9.5	39 ± 1.21
	60	1820 ± 150
40	60	22 ± 0.4
	360	42 ± 3.3
60	160	1.8 ± 0.1
	360	3.4 ± 0.1
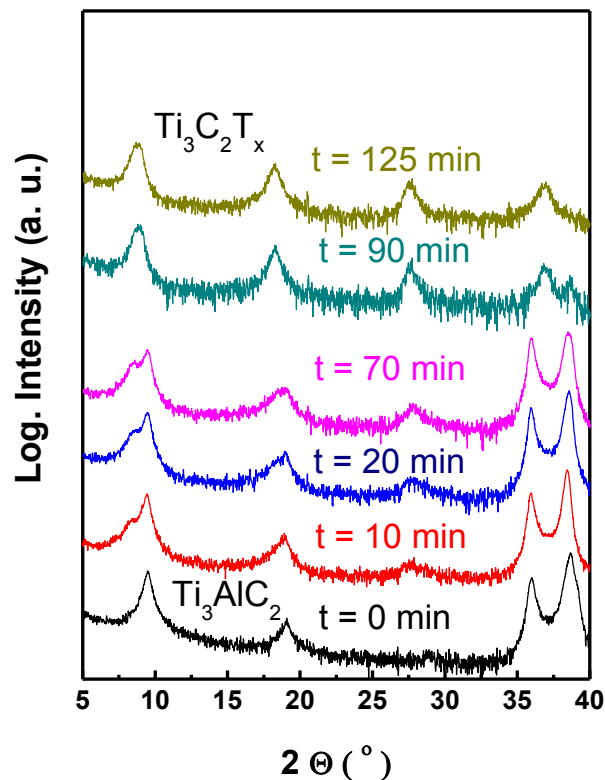
Figure S6. X-Ray diffraction patterns of 43-nm thick Ti_3AlC_2 films as a function of etching time in 50 % HF at room temperature.

VI. EDX mapping of $Ti_3C_2T_x$

Figure S7 presents an EDX map showing the distribution of C, Ti, F, and O atoms over the corresponding high-resolution STEM image of $Ti_3C_2T_x$ produced by HF etching. The fluorine signal is concentrated primarily in the spaces between the Ti-C layers, which suggests that F atoms are attached to the surfaces of the Ti-C layers.
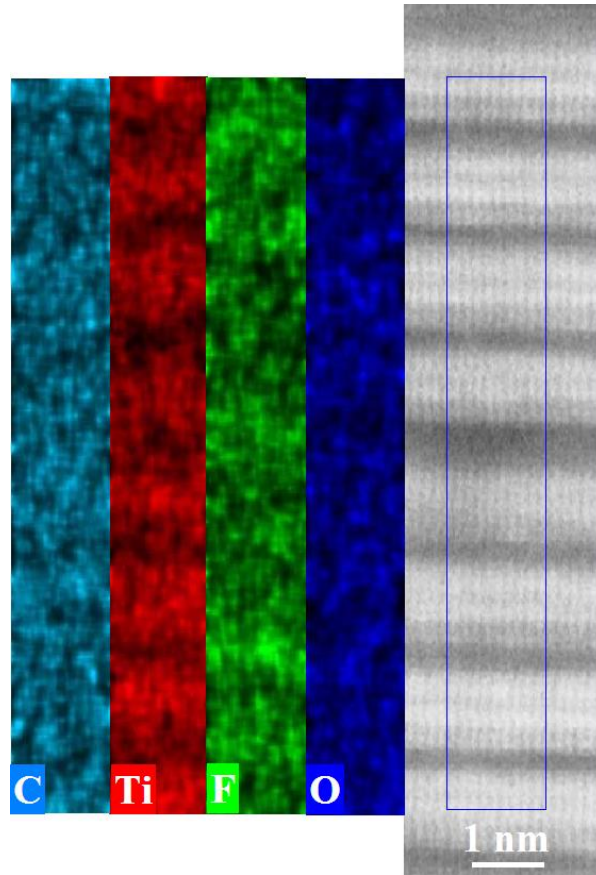
Figure S7. STEM image and EDX maps for $Ti_3C_2T_x$ of 60 nm nominal thickness.

## VII. Morphologies of Ti_3AlC_2 and $Ti_3C_2T_x$ films

Figure S8a shows the morphology of a typical Ti_3AlC_2 surface, where the hexagonal striations reflect to the symmetry of the basal planes together with some three-sided grains that are protruding out of plane due to their tilted orientations. Such nonbasal grains are preferentially etched, leading to premature over-etching and thus higher resistivities. Figure S8b shows the surface of Ti_3AlC_2 film after etching ($Ti_3C_2T_x$). Pinholes have appeared near the tilted grains in the $Ti_3C_2T_x$, presumably a result of the preferential etching of the tilted grains with respect to the grains parallel to the substrate surface.

Figures S9a,b show TEM images of the tilted grains of Ti_3AlC_2 and $Ti_3C_2T_x$, respectively. In Figure S9a, Ti_3AlC_2 grain has grown over Ti_2AlC. The nonbasal grain nucleated on the substrate and overgrew the basal grains, since growth along basal planes is faster than normal to it. For the $Ti_3C_2T_x$ grain (Figure S9b), defects appear in the interface between both the tilted and horizontal grains.

Low magnification cross-sectional TEM images of two $Ti_3C_2T_x$ films are shown in Figure S9c. The two samples are facing each other so that the surface of $Ti_3C_2T_x$ is

inwards. The globules appearing between the two films are carbon particles coming from the glue being used to hold the samples together on the TEM grid. The $Ti_3C_2T_x$ films
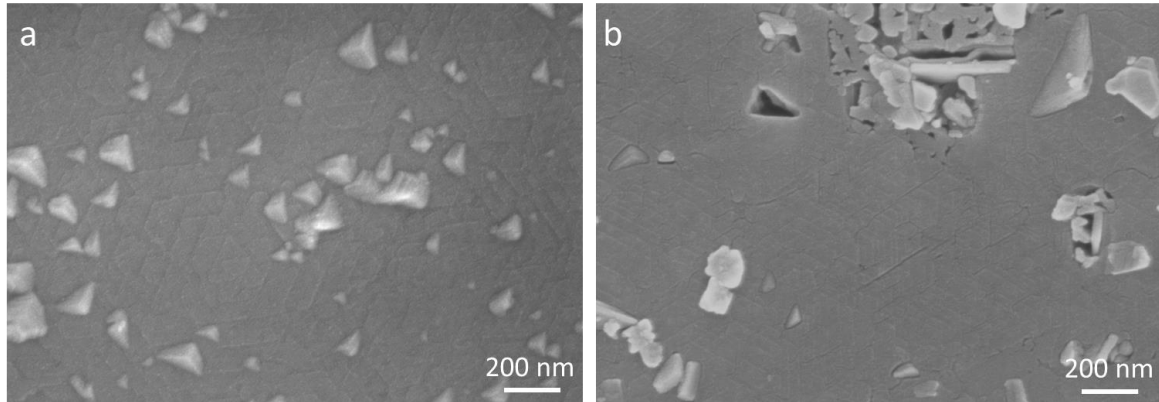
shown are uniform with some tilted grains (Figure S9a).

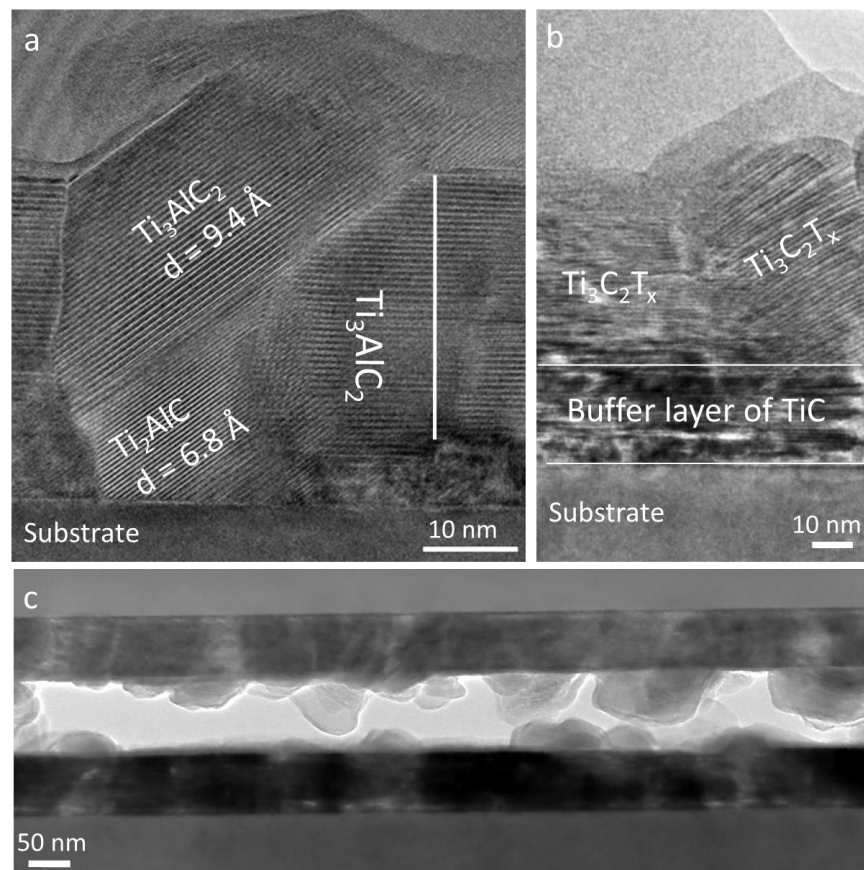**Figure S8.** SEM image of Ti_3AlC_2 and $Ti_3C_2T_x$ of 60 nm nominal thickness.

Figure S9. Cross-sectional TEM images of defective regions in Ti_3AlC_2 and $Ti_3C_2T_x$: (a) TEM image of two cross-sections of $Ti_3C_2T_x$ of 60 nm nominal thickness placed face to face. Lighter regions in the center of micrograph is the glue used during sample mounting. (b) TEM image of 60 nm thick Ti_3AlC_2 film grown on a sapphire substrate with TiC incubation layer showing a region not covered with TiC that ultimately resulted in a tilted grain of Ti_3AlC_2. (c) TEM image for $Ti_3C_2T_x$ of 60 nm nominal thickness.

14

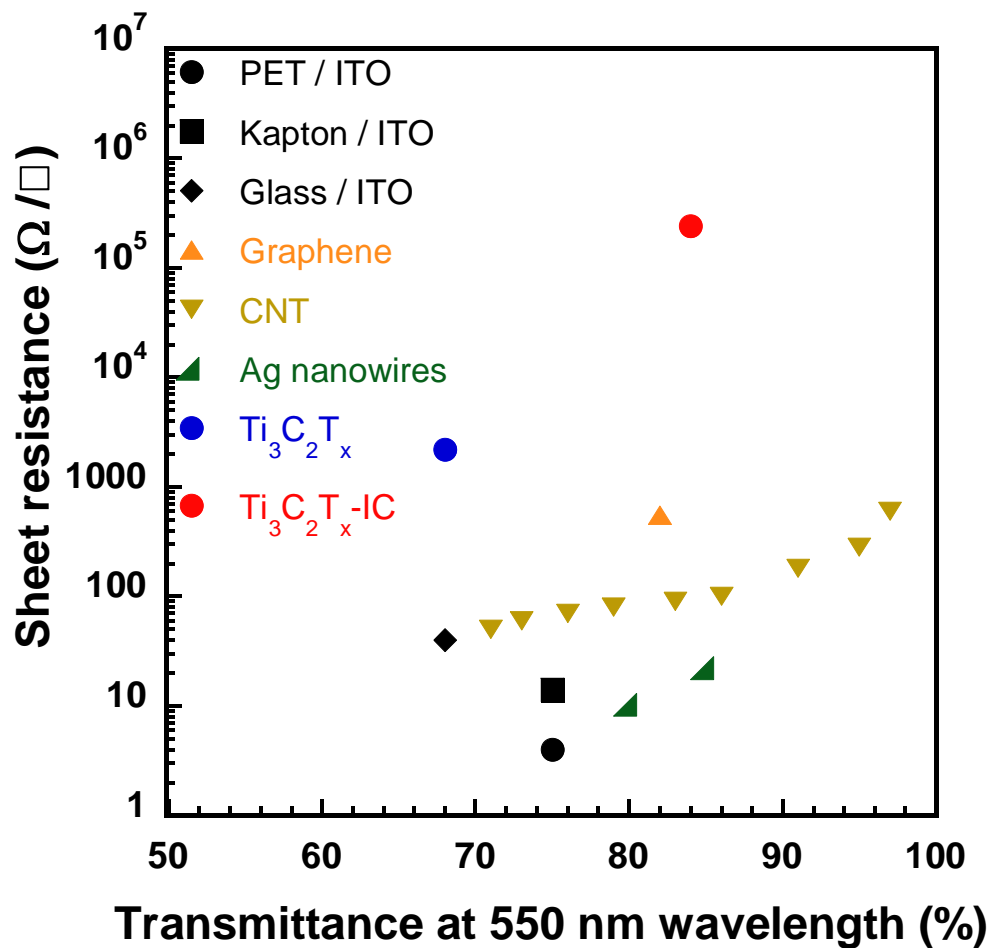## VIII. Comparison of different transparent conductive materials

Figure S10. Transmittance *vs.* sheet resistance for different transparent conductors: ITO on polyethylene terephthalate (PET), Kapton® and glass;[14] black dot, square, and rhombus respectively, graphene;[15] orange triangle, carbon nanotube (CNT);[16] gold triangles, Ag nanowires;[17] green triangles, $Ti_3C_2T_x$ of 15 nm nominal thickness; blue dot and $Ti_3C_2T_x$ of 15 nm nominal thickness; red dot.

IX. Electrical transport measurements and analysis

To understand what causes the low-temperature insulating behavior, there are numerous possible models to consider. We consider the following four models: i) thermally activated, in which case $\rho \sim \exp(E_A/kT)$; ii) 3D variable range hopping for which $\rho \sim \exp(T_0/T)^{1/4}$, iii) 2D variable range hopping for which $\rho \sim \exp(T_0/T)^{1/3}$, and, iv) a weak localization model for which $\rho \sim \ln(T)$. [18-21]

The low-temperature (< 75 K) resistivity data for $Ti_3C_2T_x$ films of 28 nm nominal thickness were fitted to all of the aforementioned models. Results of these fits are shown in Figures S10 and S11. The poor fit for the first three models to the experimental obtained (Figure S11) suggest that they can be discarded. In contradistinction, the fit for the weak-localization model is nearly perfect for all samples (insets in Figure S10). The low-temperature behavior of the resistivity is thus consistent with the weak localization model, a phenomenon typically observed in 2D metallic films. [19-21]

The negative magnetoresistance observed in the same temperature range is also consistent with the weak localization model[22]. This evidences a truly 2D behavior of the electronic transport properties of $Ti_3C_2T_x$, in that the charge carriers are confined and weakly localized within individual $Ti_3C_2T_x$ layers.
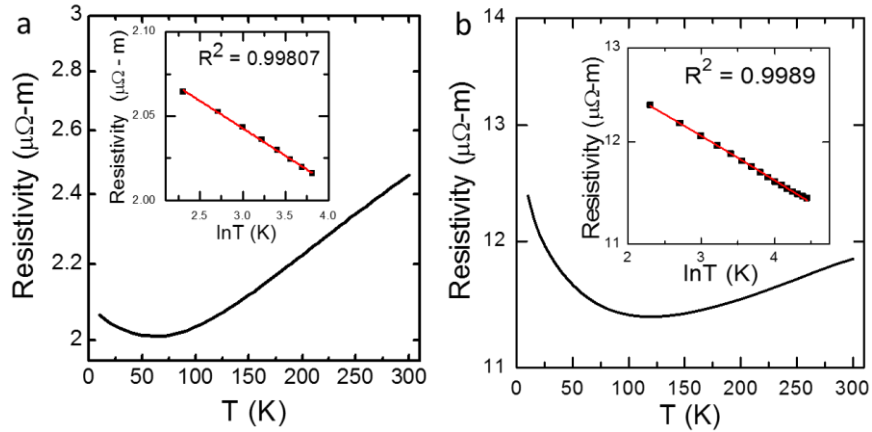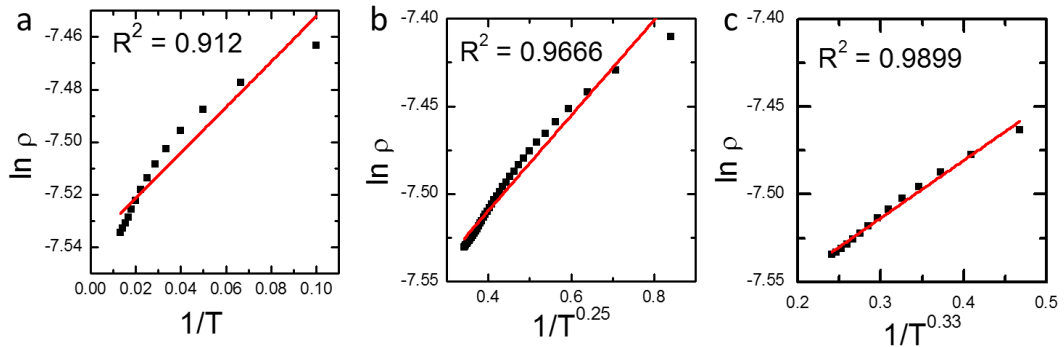

Figure S11. Temperature dependencies of electrical resistivities of a: (a) 60 nm thick $Ti_3C_2T_x$ film, (b) 28 nm thick $Ti_3C_2T_x$-IC film. Insets in both figures show the fits of resistivities, in the 2 to 74 K temperature range, to the weak localization model, viz. $\rho \sim \ln(T)$.

Figure S12. Fitting of resistivity of 28 nm nominal thickness $Ti_3C_2T_x$ films on temperature in the 2 to 74 K

temperature range assuming: (a) a thermally activated process; (b) a 3D variable range hopping model;[18] (c) 2D variable range hopping model.[18]

REFERENCES

(1) Wilhelmsson, O.; Palmquist, J.-P.; Lewin, E.; Emmerlich, J.; Eklund, P.; Persson, P.; Högberg, H.; Li, S.; Ahuja, R.; Eriksson, O. *J. Cryst. Growth* **2006**, *291,* 290-300.

(2) Myhra, S.; Crossley, J. A. A.; Barsoum, M. W., *J. Phys. Chem. Solids* **2001**, *62,* 811-817.

(3) Mencer, D. E.; Hess, T. R.; Mebrahtu, T.; Cocke, D. L.; Naugle, D. G., *J. Vac. Sci. Technol., A* **1991**, *9,* 1610-1615.

(4) Biesinger, M. C.; Lau, L. W. M.; Gerson, A. R.; Smart, R. S. C., *Appl. Surf. Sci.* **2010**, *257*, 887-898.

(5) Jayaweera, P. M.; Quah, E. L.; Idriss, H., *J. Phys. Chem. C* 2**007**, *111*, 1764-1769.

(6) Cousens, D. R.; Wood, B. J.; Wang, J. Q.; Atrens, A., *Surf. Interface Anal.* **2000**, *29*, 23-32.

(7) Mashtalir, O.; Naguib, M.; Mochalin, V. N.; Dall'Agnese, Y.; Heon, M.; Barsoum, M. W.; Gogotsi, Y., *Nat. Commun.* **2013**, *4*, 1716.

(8) Sultana, T.; Georgiev, G. L.; Auner, G.; Newaz, G.; Herfurth, H. J.; Patwa, R., *Appl. Surf. Sci.* **2008**, *255*, 2569-2573.

(9) Yamamoto, S.; Bluhm, H.; Andersson, K.; Ketteler, G.; Ogasawara, H.; Salmeron, M.; Nilsson, A., *J. Phys.: Condens. Matter* **2008**, *20*, 184025.

(10) Ernst, K. H.; Grman, D.; Hauert, R.; Hollander, E., *Surf. Interface Anal.* **1994**, *21*, 691-696.

(11) Bourbigot, S.; Le Bras, M.; Gengembre, L.; Delobel, R. *Appl. Surf. Sci.* **1994**, *81*, 299-307.

(12) Egawa, C.; Naito, S.; Tamaru, K., *Surf. Sci.* **1983**, *131*, 49-60.

(13) Naguib, M.; Kurtoglu, M.; Presser, V.; Lu, J.; Niu, J.; Heon, M.; Hultman, L.; Gogotsi, Y.; Barsoum, M. W., *Adv. Mater.* **2011**, *23*, 4248-4253.

(14) Herrero, J.; Guillén, C., *Vacuum* **2002**, *67*, 611-616.

(15) Bae, S.; Kim, H.; Lee, Y.; Xu, X.; Park, J.-S.; Zheng, Y.; Balakrishnan, J.; Lei, T.; Kim, H. R.; Song, Y. I., *Nat. Nanotechnol.* **2010**, *5*, 574-578.

(16) Geng, H.-Z.; Kim, K. K.; So, K. P.; Lee, Y. S.; Chang, Y.; Lee, Y. H., *J. Am. Chem. Soc.* **2007**, *129*, 7758-7759.

(17) Lee, J.-Y.; Connor, S. T.; Cui, Y.; Peumans, P., *Nano Lett.* **2008**, *8*, 689-692.

(18) Yu, D.; Wang, C.; Wehrenberg, B. L.; Guyot-Sionnest, P., *Phys. Rev. Lett.* **2004**, *92*, 216802.

(19) Bergmann, G., *Phys Rev B* **1982**, *25*, 2937-2939.

(20) Bergmann, G., *Phys. Rep.* **1984**, *107*, 1-58.

(21) Shih, C.-J.; Vijayaraghavan, A.; Krishnan, R.; Sharma, R.; Han, J.-H.; Ham, M.-H.; Jin, Z.; Lin, S.; Paulus, G. L.; Reuel, N. F., *Nat. Nanotechnol.* **2011**, *6*, 439-445.

(22) Henzler, M.; Lüer, T.; Heitmann, J., *Phys Rev B* **1999**, *59*, 2383-2387.